

Measurement of the cosmic ray proton and helium spectrum with energy above 100TeV by the LHAASO experiment

Ma Lingling,^{a,c} Wang Yudong,^{a,c} Wang Liping,^{a,d} Yin Liqiao,^{a,c} You Zhiyong,^{a,b,c} and Zhang Shoushan^{a,c} on behalf of the LHAASO

Collaboration

(a complete list of authors can be found at the end of the proceedings)

^aThe Institute of High Energy Physics of the Chinese Academy of Sciences,
YuQuan Road.19B, shijingshan district, Beijing, China

^bUniversity of Chinese Academy of Sciences, Department,
YuQuan Road.19A, shijingshan district, Beijing, China

^cTIANFU Cosmic Ray Research Center,
Chengdu, Sichuan, China

^dShandong University,
Qingdao, Shandong, China
E-mail: youzhiyong@ihep.ac.cn, wangyd89@ihep.ac.cn,
yinlq@ihep.ac.cn, wanglp@ihep.ac.cn

Large High Altitude Air Shower Observatory (LHAASO) consists of three interconnected detectors with the aim to measure several air shower characteristics simultaneously. One of the main scientific goals is to measure the individual cosmic ray spectrum at knee regime. In this paper we introduce the progress of measuring the energy spectrum of proton and helium composition of cosmic rays. According to the number of Cherenkov photons recorded by WFCTA, the energies can be reconstructed and the resolution can achieve 15% for showers produced by protons and helium with energies above 300 TeV. Due to the hybrid observation to the air showers, several parameters can be used to identify the mass compositions of the air shower. The ability of LHAASO to identify the mass composition are studied in detail in the paper.

37th International Cosmic Ray Conference (ICRC 2021)
July 12th – 23rd, 2021
Online – Berlin, Germany

1. Introduction

The measurement of individual cosmic ray spectra especially near the "knee" region is important to investigate cosmic ray acceleration and propagation mechanisms. One of main scientific goals of the Large High Altitude Air Shower Observatory (LHAASO) [1, 2] is to measure the single element energy spectrum with energies from 30 TeV to several EeV.

LHAASO is located on Mountain Haizi, 4410 m above sea level Daocheng, in Sichuan province, China. The Water Cherenkov Detector Array (WCDA) located in the center of the LHAASO site. It consists of three water ponds with a total area of 78,000 m² and a water depth 4.5 m. At the bottom of each union, two types of PMTs are installed watching upward to cover a wide dynamic range spanning from 1 to 200,000 photo-electrons which are generated by the Cherenkov photons produce in water by the secondary charged particles in the air shower. The wide dynamic range make sure WCDA can measure air showers with energy from TeV to 10 PeV without any saturation. The Kilometer Square Array (KM2A) consists of 5,195 scintillation counters (ED) and 1,188 under surface muon detectors (MD). Both EDs and MDs cover an area of 1 km², plus a 0.3 km² skirt array to identify shower with cores falling outside the central area. The half KM2A array which includes 2,365 EDs and 584 MDs has been operated stably since 27 December 2019. With the large aperture, KM2A can detect cosmic rays with energies from 100 TeV to 100 PeV. The Wide Field of View Cherenkov Telescope Array (WFCTA) consists of 18 telescopes which are installed near WCDA to achieve hybrid observation. Each telescope mainly consists of a spherical mirror and a camera which are installed in a cargo container. The camera is made up of a 32 × 32 SiPMs array with a field of view 0.5° × 0.5° for each pixel and a total field of view 16° × 16°. The telescope can adjust its pointing and position for different energy spectral measurement aims. So WFCTA can cover the energy range from 10 TeV to 100 PeV by adjust its pointing and arrangement. For the measurement of proton and helium spectrum, the first six telescopes with the main optical axis pointing to the zenith angle 30° are used.

In Section 2, the hybrid events is introduced. In Section 3, reconstruction of EAS is introduced. It is shown that the energy resolution of WFCTA for proton and helium composition is 15% above 300 TeV, and the resolution of shower maximum of secondary particles (X_{max}) is about 38 g/cm². In Section 4, several component sensitive parameters are represented. Section 5 is conclusion and discussion.

2. Experiment data

The three detector arrays are triggered independently with the White Rabbit clock system. The data can be merged offline through the absolute trigger time. This paper focuses on the measurement of the light component energy spectrum of cosmic rays. WFCTA provides energy information. KM2A or WCDA provides shower geometry information. Therefore, based on events that triggered WFCTA, it can be merged by KM2A or WCDA triggered events. The analysis methods can be different for showers that fall on different positions in LHAASO.

When the shower falls on WCDA, the surrounding KM2A can provide electromagnetic particle and muon information. In this scene, events triggering the three detector arrays are merged. When the shower falls on KM2A, limited by the relative location and area of WCDA, it does not much

help to particle identification and geometry reconstruction. So events just triggered WFCTA and KM2A are merged.

In this talk, two hybrid events data set mentioned above are counted. In the first data set, the statistical time is from November 5th, 2020 to March 3rd, 2021. For the statistics of observation time, the following conditions should be met:

1. Good weather selecting condition. The definition of good weather is that the infrared brightness temperature of infrared cloud instrument is less than -65°C .
2. Moon less condition. The space angle between the telescope and the moon is larger than 30° .
3. WFCTA working condition. The working current of the SiPM camera should be less than 1.5 A and high voltage is large than 75 V.
4. WCDA working condition. In the range of 83 ± 15 kHz in 60 s, WCDA is considered to work normally.
5. KM2A working condition. In the range of 1.8 ± 0.15 kHz in 60 s, KM2A is considered to work normally.

After selection of the above conditions, the effective hybrid observation time is 750 hours. Meanwhile, the amount of hybrid events is counted. Two selection conditions are adopted to Cherenkov image:

1. After Cherenkov image cleaning, the remaining pixels are larger than 10, namely above 100 TeV.
2. The center of gravity of the image is $6^{\circ} \times 6^{\circ}$ of FOV.

The cumulative amount of data is 12 million. Average event rate of a day versus time is shown in Figure 1(a). The fluctuations are strongly correlated with the moon phase, as can be noticed by comparing the moon phase given in the lower graph for the same time period.

For hybrid events of WFCTA and KM2A, the statistical time is from November 5th, 2020 to April 15th, 2021. The selection conditions are consistent with the above items except the WCDA working condition. The effective hybrid observation time is 970 hours with 22.4 million hybrid events. Average event rate of a day versus time is shown in Figure 1(b).

3. Shower Reconstruction

3.1 Geometry Reconstruction

Since six telescopes of WFCTA point to different directions, they cannot reconstruct the core location and arrival direction of the air shower well. Both KM2A and WCDA are ground-based detector arrays. They record the time and energy relevant information of secondary particles of a shower. The time resolutions of WCDA and ED are 1 ns and 2 ns, respectively[3, 4]. As a result, they can provide precision measurements for shower core and direction. For KM2A, only ED hits are used to reconstruct core location and arrival direction. The core resolution and angular resolution of KM2A half-array is 3 m and 0.3° at 100TeV[3]. As for WCDA, they are 3 m above and 0.2° above 10 TeV[4].

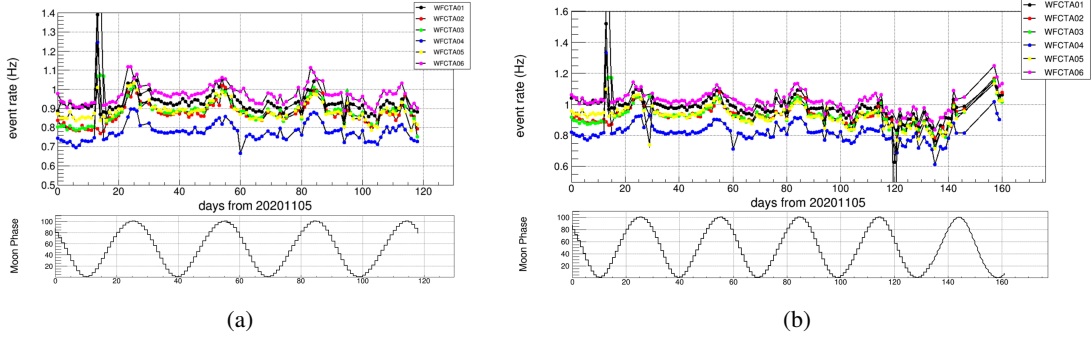


Figure 1: (a) Average event rate of hybrid observation of WFCTA, WCDA and KM2A versus time. (b) Average event rate of hybrid observation of WFCTA and KM2A versus time.

3.2 Cherenkov Image Reconstruction

Secondary particles are mostly extremely relativistic and will generate Cherenkov radiation when they passing through the atmosphere. Only particles whose energy exceed the threshold energy E_{th} can produce Cherenkov radiation, and the photon production is related to air density and particle energy. The angular distribution of produced Cherenkov photons with respect to the shower axis is well parameterised as a function of height and shower age[5].

With a spherical mirror, WFCTA can image Cherenkov photons on a focal plane where a SiPM camera is equipped. A parameterisation method to describe the image on the camera is reported by Hillas [6]. The image axis on the camera corresponds to the shower axis in space, and each point on the image axis corresponds to a certain direction from telescope to the shower axis. A plane through the detector and the shower axis (SDP) is naturally established. Fig. 2(a) is longitudinal Cherenkov photon profile of an proton event in CORSIKA, whose energy is 396 TeV, X_{max} is 530 g/cm² and perpendicular distance from telescope to shower axis (R_p) is 98 m. Dividing the Cherenkov image into bins of 0.1° along the image axis and after smoothing, an angular profile of number of photons is obtained (see Fig. 2(b)). Fig. 2(c) shows the atmospheric depth of photons in slice from 1.0° to 5.0°. Most of photons in 1.0° (max signal layer) come from the air depth of 230~370 g/cm² (air depth before X_{max}).

As shown in Fig. 2(c), the angular distribution of the signals on the camera plane reflects the longitudinal development of Cherenkov radiation. A function convolving the Landau distribution with a normal distribution of variance σ_g

$$f(x, \Delta, MPV, A, \sigma_g) = A \int_{-\infty}^{+\infty} Landau(x', \Delta, MPV) \times Gaus(x', \sigma_g) dx' \quad (1)$$

is used to fit the angular distribution of photons along image axis detected by telescope. Here, Δ and MPV is scaling and location parameter of Landau density, respectively. A is normalization constant.

3.3 Energy Reconstuction

The parameter A in function (1) which represents the total size of Cherenkov photons detected by WFCTA is related to primary energy. The lateral distribution of Cherenkov light at the altitude of

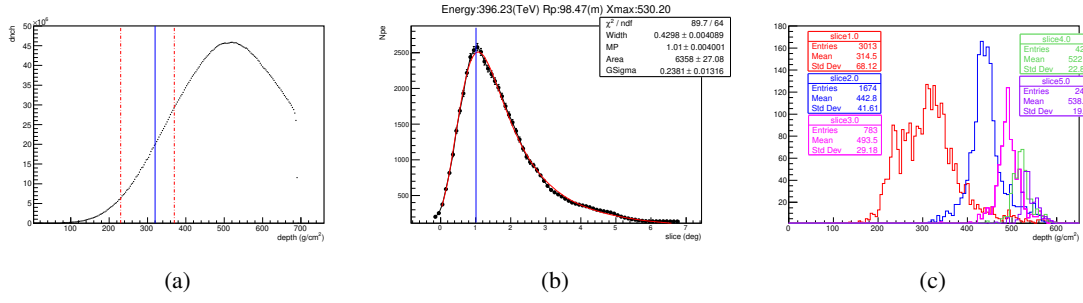


Figure 2: (a) Longitudinal distribution of Cherenkov photons in CORSIKA. (b) Angular distribution of number of photons on WFCTA. X axis is angular distance from arrival direction along the image axis. The zero point stands for the arriving direction of the shower. The layer of the maximum signal is around 1.0° . (c) Atmospheric depth of photons in slice of 1.0° , 2.0° , 3.0° , 4.0° and 5.0° .

LHAASO is still very steep. Thus the parameter A is also related to R_p . An energy reconstruction table that contains two parameters (R_p and A) is created by using simulation events of proton and helium composition based on Gassier model (see Fig 3(a)). Fig 3(b) shows the energy resolution and bias of reconstructed by WFCTA. The energy resolution is about 15% above 300 TeV, and the energy bias is less than 2%.

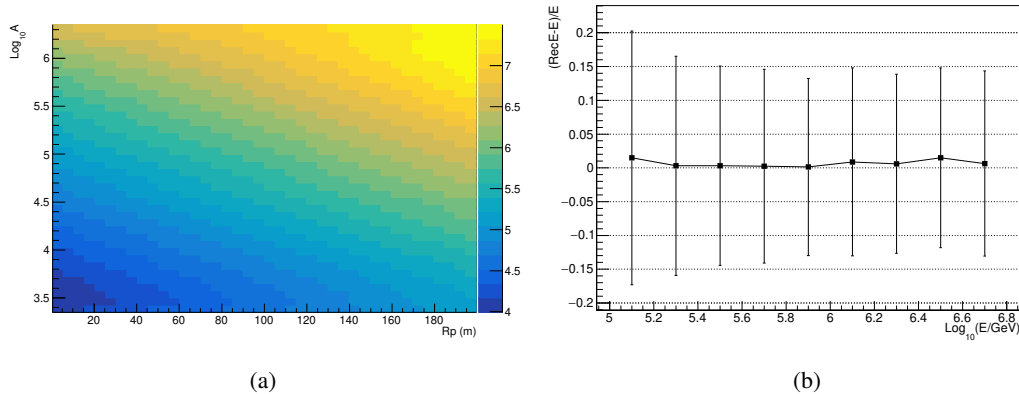


Figure 3: (a) Energy reconstruction table of proton and helium based on Gassier model. The X axis is R_p and Y axis is $\text{Log}_{10} A$, the color represents the primary energy in log scale. (b) The dependence of energy resolution of proton and helium composition on each reconstructed energy bin. The squares stand for energy bias and the error bars are for energy resolution.

3.4 Shower Maximum

As mentioned before, the angular profile of photons on camera reflects the longitudinal development of Cherenkov photons to a certain extent. The scaling parameter Δ in function (1) is related to shower maximum and R_p . Separating events in different R_p bins, the X_{max} can be reconstructed with Δ . The resolution of reconstruction of X_{max} improves with energy and reaches 38 g/cm^2 at 1 PeV, but with a bias of about 10 g/cm^2 (see Fig 4).

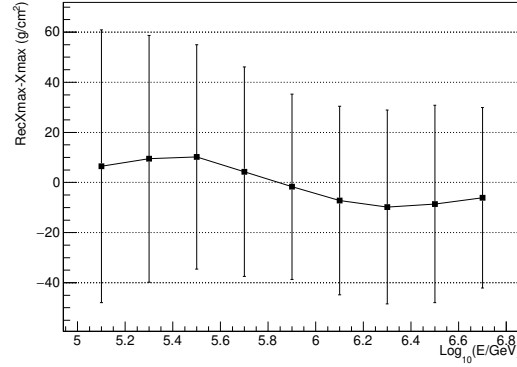


Figure 4: X_{max} resolution over different energies. The squares stand for X_{max} bias and the error bars are for X_{max} resolution.

4. Composition Sensitive Parameters

LHAASO has several kinds of detectors, complementary techniques can be achieved to measure simultaneously many parameters composition models dependent. Detailed simulations including air shower simulations and detector responses are done in detail to study the ability of the hybrid observation to identify the mass compositions. QGSJETII04 are selected to describe the hadronic interaction for energies above 100GeV, while FLUKA is selected to describe the hadronic interaction for energies below 100 GeV. Five composition groups (proton, helium, CNO, MgAlSi, iron) are simulated with energies from 10 TeV to 10 PeV. During the analysis, the proton and helium are considered as light component, the other three mass composition groups are considered as heavy component.

4.1 Extension Rate (<ER>) from WCDA

WCDA is a full coverage detector. It can provide precision detection of shower core region and lateral distribution of secondary particles. For a shower produced by proton and helium, the lateral distribution of secondary particles is flatter than that of heavier nuclei. $\langle ER \rangle = \frac{\sum (R_i \times P e_i)}{\sum P e_i}$ is used as discrimination parameter, where R_i is the perpendicular distance from i_{th} cell to shower axis and $P e_i$ is signal of this cell. $\langle ER \rangle$ is also related to the primary energy. Fig 5(a) shows the distribution of $\langle ER \rangle$ after energy correction. The events selection criteria follows as, the core location is limited in 60 m from center of WCDA-1, the signal of brightest cell is bigger than 4000 number of electronphotons, and the near core region (10 m from shower core) accounts for more than 30% of total size in the region of 30 m from shower core.

4.2 Length and width ratio $\frac{L}{W}$ of Cherenkov image

The shape of Cherenkov photon image is also a mass sensitive parameter. The shape of the Cherenkov photon image can be described by an ellipse. The major axis (Length) and minor axis (Width) of the ellipse reflect the development of the air showers. For showers developed deeper, the shapes of the image are more elliptic, so the ratio of the Length and Width ($\frac{L}{W}$) of the image

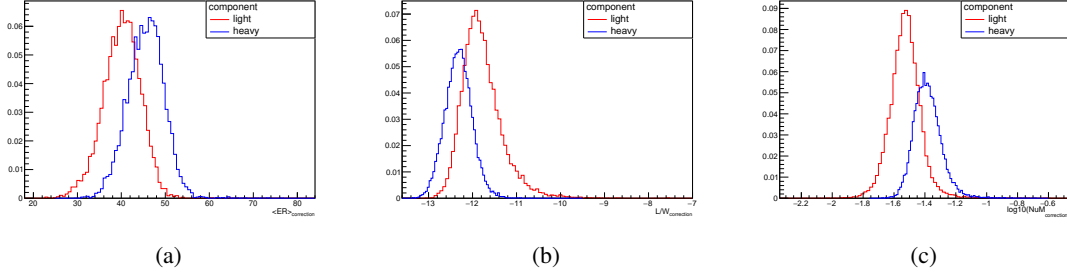


Figure 5: (a) Distribution of $\langle ER \rangle$ after energy correction. (b) Distribution of $\frac{L}{W}$ after Rp and size correction. (c) Distribution of number of muons after energy correction. In all three panels, the red line represents shower initiated by light component, and blue for heavy component.

is a parameter relative to the depth of the shower maximum, which is sensitive to the primary mass compositions of the air showers. In addition, the shape of the image also depends on the Rp and the primary energy of the air shower. So it is necessary to make Rp correction and energy correction to $\frac{L}{W}$ before identify mass composition of cosmic rays.

In order to make sure the Cherenkov image are fully recorded, the gravity center of the image are selected as $|X| < 5^\circ$, and $|Y| < 5^\circ$, the number of pixels after image cleaning should be larger than 10 ($N_{pix} > 10$). For showers with Rp less than 50 m, the shape of the Cherenkov image is more like a circular. Moreover, showers with Rp larger than 150 m, the trigger efficiency is too low. So the events with $50 \text{ m} < R_p < 150 \text{ m}$ are selected. With these cuts, the distributions of the corrected $\frac{L}{W}$ are shown in Fig.5(b)

4.3 Number of muon from KM2A

In recent years, informations of muon have always been one of the focus of the identification of the mass composition of cosmic rays. The muons mainly come from the decay of charged pions (π^+, π^-), kaons (K^+, K^-, K_L^0), and other charmed particles, such as $D^\pm, D^0, J/\psi$, which are produced mainly in the forward region of the center of mass of the first few interactions. The number of muon (N_μ) in air shower is directly related to the composition of cosmic rays, and at the same time is related to the primary particle energy. So the number of muon in the air showers plays an important role in the study of mass composition of cosmic rays. Due to the Number of muons are affected by the primary energy of the air shower, the number of muons should be corrected by the shower's energy. The total number of muons recorded by the MDs within a ring with radius from 30 m to 380 m from the shower core denoted as the number of muons N_{um} of the shower. In order to make sure high quality of the reconstructions of the air shower, the showers with cores located in the KM2A are should be selected. The number of particles detected by EDs within a circle with radius 100m from shower core is more than twice of that within a ring with radius from 40 m to 100 m. With these cuts, the distributions of corrected N_{um} is shown in Fig.5(c).

5. Conclusion and Discussion

The hybrid observation of the three type detectors has been achieved by offline. Two data sets with high statistics (12 million events for the first data set and 22.4 million events for the second data set) and good qualities selection criteria are obtained based on the core positions of the air showers. Moreover, the energy reconstruction and mass composition identification are studied by simulations. The resolution of energy reconstruction can be obtained 15% for protons and helium nuclei with energies above 300 TeV by the total Cherenkov photons recorded by WFCTA. The parameters which are sensitive to the mass compositions are studied according to the characteristics of the air showers, such as the extension rate $\langle ER \rangle$ of the air shower, the ratio of the length and the width ($\frac{L}{W}$) of the Cherenkov image, the number of muons ($N_{\mu m}$) in the air shower. According to our study, all of the three parameters can identify the mass composition of cosmic rays effectively. The effects of the hadronic models to the energy reconstruction and mass composition will be studied in the future.

6. Acknowledgements

This work is supported by the National Key R&D Program of China (No. 2018YFA0404201), (No. 2018YFA0404202). This work is also supported in China by the Key Laboratory of Particle Astrophysics, Institute of High Energy Physics, CAS. Projects No. 11475190 and No. 11675204 of NSFC also provide support to this study.

References

- [1] Z. Cao et al., Chinese Physics C 34, 249 (2010)
- [2] H.H. He et al., LHAASO Project: detector design and prototype, 31st ICRC, LODZ, (2009)
- [3] F. Aharonian et al 2021 Chinese Phys. C 45 025002
- [4] F. Aharonian et al. arXiv:2101.03508v1 [astro-ph.IM]
- [5] F. Nerling, et al., Astropart. Phys. 24 (2006) 421.
- [6] Hillas, A. 1985, 19th ICRC V3, 445-448.

Full Authors List: LHAASO Collaboration

Zhen Cao^{1,2,3}, F. Aharonian^{4,5}, Q. An^{6,7}, Axikegu⁸, L.X. Bai⁹, Y.X. Bai^{1,3}, L.X. Bai⁹, Y.X. Bai^{1,3}, Y.W. Bao¹⁰, D. Bastieri¹¹, X.J. Bi^{1,2,3}, Y.J. Bi^{1,3}, H. Cai¹², J.T. Cai¹¹, Zhe Cao^{6,7}, J. Chang¹³, J.F. Chang^{1,3,6}, B.M. Chen¹⁴, E.S. Chen^{1,2,3}, J. Chen⁹, Liang Chen^{1,2,3}, Liang Chen¹⁵, Long Chen⁸, M.J. Chen^{1,3}, M.L. Chen^{1,3,6}, Q.H. Chen⁸, S.H. Chen^{1,2,3}, S.Z. Chen^{1,3}, T.L. Chen¹⁶, X.L. Chen^{1,2,3}, Y. Chen¹⁰, N. Cheng^{1,3}, Y.D. Cheng^{1,3}, S.W. Cui¹⁴, X.H. Cui¹⁷, Y.D. Cui¹⁸, B. D’Ettorre Piazzoli¹⁹, B.Z. Dai²⁰, H.L. Dai^{1,3,6}, Z.G. Dai⁷, Danzengluobu¹⁶, D. della Volpe²¹, X.J. Dong^{1,3}, K.K. Duan¹³, J.H. Fan¹¹, Y.Z. Fan¹³, Z.X. Fan^{1,3}, J. Fang²⁰, K. Fang^{1,3}, C.F. Feng²², L. Feng¹³, S.H. Feng^{1,3}, Y.L. Feng¹³, B. Gao^{1,3}, C.D. Gao²², L.Q. Gao^{1,2,3}, Q. Gao¹⁶, W. Gao²², M.M. Ge²⁰, L.S. Geng^{1,3}, G.H. Gong²³, Q.B. Gou^{1,3}, M.H. Gu^{1,3,6}, F.L. Guo¹⁵, J.G. Guo^{1,2,3}, X.L. Guo⁸, Y.Q. Guo^{1,3}, Y.Y. Guo^{1,2,3,13}, Y.A. Han²⁴, H.H. He^{1,2,3}, H.N. He¹³, J.C. He^{1,2,3}, S.L. He¹¹, X.B. He¹⁸, Y. He⁸, M. Heller²¹, Y.K. Hor¹⁸, C. Hou^{1,3}, H.B. Hu^{1,2,3}, S. Hu⁹, S.C. Hu^{1,2,3}, X.J. Hu²³, D.H. Huang⁸, Q.L. Huang^{1,3}, W.H. Huang²², X.T. Huang²², X.Y. Huang¹³, Z.C. Huang⁸, F. Ji^{1,3}, X.L. Ji^{1,3,6}, H.Y. Jia⁸, K. Jiang^{6,7}, Z.J. Jiang²⁰, C. Jin^{1,2,3}, T. Ke^{1,3}, D. Kuleshov²⁵, K. Levochkin²⁵, B.B. Li¹⁴, Cheng Li^{6,7}, Cong Li^{1,3}, F. Li^{1,3,6}, H.B. Li^{1,3}, H.C. Li^{1,3}, H.Y. Li^{7,13}, J. Li^{1,3,6}, K. Li^{1,3}, W.L. Li²², X.R. Li^{1,3}, Xin Li^{6,7}, Xin Li⁸, Y. Li⁹, Y.Z. Li^{1,2,3}, Zhe Li^{1,3}, Zhuo Li²⁶, E.W. Liang²⁷, Y.F. Liang²⁷, S.J. Lin¹⁸, B. Liu⁷, C. Liu^{1,3}, D. Liu²², H. Liu⁸, H.D. Liu²⁴, J. Liu^{1,3}, J.L. Liu²⁸, J.S. Liu¹⁸, J.Y. Liu^{1,3}, M.Y. Liu¹⁶, R.Y. Liu¹⁰, S.M. Liu⁸, W. Liu^{1,3}, Y. Liu¹¹, Y.N. Liu²³, Z.X. Liu⁹, W.J. Long⁸, R. Lu²⁰, H.K. Lv^{1,3}, B.Q. Ma²⁶, L.L. Ma^{1,3}, X.H. Ma^{1,3}, J.R. Mao²⁹, A. Masood⁸, Z. Min^{1,3}, W. Mitthumsiri³⁰, T. Montaruli²¹, Y.C. Nan²², B.Y. Pang⁸, P. Pattarakijwanich³⁰, Z.Y. Pei¹¹, M.Y. Qi^{1,3}, Y.Q. Qi¹⁴, B.Q. Qiao^{1,3}, J.J. Qin⁷, D. Ruffolo³⁰, V. Rulev²⁵, A. Sáiz³⁰, L. Shao¹⁴, O. Shchegolev^{25,31}, X.D. Sheng^{1,3}, J.Y. Shi^{1,3}, H.C. Song²⁶, Yu.V. Stenkin^{25,31}, V. Stepanov²⁵, Y. Su³², Q.N. Sun⁸, X.N. Sun²⁷, Z.B. Sun³³, P.H.T. Tam¹⁸, Z.B. Tang^{6,7}, W.W. Tian^{2,17}, B.D. Wang^{1,3}, C. Wang³³, H. Wang⁸, H.G. Wang¹¹, J.C. Wang²⁹, J.S. Wang²⁸, L.P. Wang²², L.Y. Wang^{1,3}, R.N. Wang⁸, W. Wang¹⁸, W. Wang¹², X.G. Wang²⁷, X.J. Wang^{1,3}, X.Y. Wang¹⁰, Y. Wang⁸, Y.D. Wang^{1,3}, Y.J. Wang^{1,3}, Y.P. Wang^{1,2,3}, Z.H. Wang⁹, Z.X. Wang²⁰, Zhen Wang²⁸, Zheng Wang^{1,3,6}, D.M. Wei¹³, J.J. Wei¹³, Y.J. Wei^{1,2,3}, T. Wen²⁰, C.Y. Wu^{1,3}, H.R. Wu^{1,3}, S. Wu^{1,3}, W.X. Wu⁸, X.F. Wu¹³, S.Q. Xi^{1,3}, J. Xia^{7,13}, J.J. Xia⁸, G.M. Xiang^{2,15}, D.X. Xiao¹⁶, G. Xiao^{1,3}, H.B. Xiao¹¹, G.G. Xin¹², Y.L. Xin⁸, Y. Xing¹⁵, D.L. Xu²⁸, R.X. Xu²⁶, L. Xue²², D.H. Yan²⁹, J.Z. Yan¹³, C.W. Yang⁹, F.F. Yang^{1,3,6}, J.Y. Yang¹⁸, L.L. Yang¹⁸, M.J. Yang^{1,3}, R.Z. Yang⁷, S.B. Yang²⁰, Y.H. Yao⁹, Z.G. Yao^{1,3}, Y.M. Ye²³, L.Q. Yin^{1,3}, N. Yin²², X.H. You^{1,3}, Z.Y. You^{1,2,3}, Y.H. Yu²², Q. Yuan¹³, H.D. Zeng¹³, T.X. Zeng^{1,3,6}, W. Zeng²⁰, Z.K. Zeng^{1,2,3}, M. Zha^{1,3}, X.X. Zhai^{1,3}, B.B. Zhang¹⁰, H.M. Zhang¹⁰, H.Y. Zhang²², J.L. Zhang¹⁷, J.W. Zhang⁹, L.X. Zhang¹¹, Li Zhang²⁰, Lu Zhang¹⁴, P.F. Zhang²⁰, P.P. Zhang¹⁴, R. Zhang^{7,13}, S.R. Zhang¹⁴, S.S. Zhang^{1,3}, X. Zhang¹⁰, X.P. Zhang^{1,3}, Y.F. Zhang⁸, Y.L. Zhang^{1,3}, Yi Zhang^{1,13}, Yong Zhang^{1,3}, B. Zhao⁸, J. Zhao^{1,3}, L. Zhao^{6,7}, L.Z. Zhao¹⁴, S.P. Zhao^{13,22}, F. Zheng³³, Y. Zheng⁸, B. Zhou^{1,3}, H. Zhou²⁸, J.N. Zhou¹⁵, P. Zhou¹⁰, R. Zhou⁹, X.X. Zhou⁸, C.G. Zhu²², F.R. Zhu⁸, H. Zhu¹⁷, K.J. Zhu^{1,2,3,6} and X. Zuo^{1,3}

- ¹Key Laboratory of Particle Astrophysics & Experimental Physics Division & Computing Center, Institute of High Energy Physics, Chinese Academy of Sciences, 100049 Beijing, China.
- ²University of Chinese Academy of Sciences, 100049 Beijing, China.
- ³TIANFU Cosmic Ray Research Center, Chengdu, Sichuan, China.
- ⁴Dublin Institute for Advanced Studies, 31 Fitzwilliam Place, 2 Dublin, Ireland.
- ⁵Max-Planck-Institut für Nuclear Physics, P.O. Box 103980, 69029 Heidelberg, Germany.
- ⁶State Key Laboratory of Particle Detection and Electronics, China.
- ⁷University of Science and Technology of China, 230026 Hefei, Anhui, China.
- ⁸School of Physical Science and Technology & School of Information Science and Technology, Southwest Jiaotong University, 610031 Chengdu, Sichuan, China.
- ⁹College of Physics, Sichuan University, 610065 Chengdu, Sichuan, China.
- ¹⁰School of Astronomy and Space Science, Nanjing University, 210023 Nanjing, Jiangsu, China.
- ¹¹Center for Astrophysics, Guangzhou University, 510006 Guangzhou, Guangdong, China.
- ¹²School of Physics and Technology, Wuhan University, 430072 Wuhan, Hubei, China.
- ¹³Key Laboratory of Dark Matter and Space Astronomy, Purple Mountain Observatory, Chinese Academy of Sciences, 210023 Nanjing, Jiangsu, China.
- ¹⁴Hebei Normal University, 050024 Shijiazhuang, Hebei, China.
- ¹⁵Key Laboratory for Research in Galaxies and Cosmology, Shanghai Astronomical Observatory, Chinese Academy of Sciences, 200030 Shanghai, China.
- ¹⁶Key Laboratory of Cosmic Rays (Tibet University), Ministry of Education, 850000 Lhasa, Tibet, China.
- ¹⁷National Astronomical Observatories, Chinese Academy of Sciences, 100101 Beijing, China.
- ¹⁸School of Physics and Astronomy & School of Physics (Guangzhou), Sun Yat-sen University, 519000 Zhuhai, Guangdong, China.
- ¹⁹Dipartimento di Fisica dell’Università di Napoli ‘Federico II’, Complesso Universitario di Monte Sant’Angelo, via Cinthia, 80126 Napoli, Italy.
- ²⁰School of Physics and Astronomy, Yunnan University, 650091 Kunming, Yunnan, China.
- ²¹Departement de Physique Nucleaire et Corpusculaire, Faculte de Sciences, Universite de Gen’ev, 24 Quai Ernest Ansermet, 1211 Geneva, Switzerland.
- ²²Institute of Frontier and Interdisciplinary Science, Shandong University, 266237 Qingdao, Shandong, China.
- ²³Department of Engineering Physics, Tsinghua University, 100084 Beijing, China.
- ²⁴School of Physics and Microelectronics, Zhengzhou University, 450001 Zhengzhou, Henan, China.
- ²⁵Institute for Nuclear Research of Russian Academy of Sciences, 117312 Moscow, Russia.

POS (ICRC2021) 377

²⁶School of Physics, Peking University, 100871 Beijing, China.

²⁷School of Physical Science and Technology, Guangxi University, 530004 Nanning, Guangxi, China.

²⁸Tsung-Dao Lee Institute & School of Physics and Astronomy, Shanghai Jiao Tong University, 200240 Shanghai, China.

²⁹Yunnan Observatories, Chinese Academy of Sciences, 650216 Kunming, Yunnan, China.

³⁰Department of Physics, Faculty of Science, Mahidol University, 10400 Bangkok, Thailand.

³¹Moscow Institute of Physics and Technology, 141700 Moscow, Russia.

³²Key Laboratory of Radio Astronomy, Purple Mountain Observatory, Chinese Academy of Sciences, 210023 Nanjing, Jiangsu, China.

³³National Space Science Center, Chinese Academy of Sciences, 100190 Beijing, China.